Letter

Generating axial magnetic fields via two plasmon decay driven by a twisted laser

Yu Ji,[1] Chang-Wang Lian,[2,3] Yin Shi,[2] Rui Yan,[1,4,*] Shihui Cao,[5] Chuang Ren,[5,6] and Jian Zheng[2,4]

[1]*Department of Modern Mechanics, University of Science and Technology of China, Hefei 230026, China*
[2]*Department of Plasma Physics and Fusion Engineering, University of Science and Technology of China, Hefei, Anhui 230026, China*
[3]*Laser Fusion Research Center, China Academy of Engineering Physics, Sichuan, Mianyang 621900, China*
[4]*Collaborative Innovation Center of IFSA (CICIFSA), Shanghai Jiao Tong University, Shanghai 200240, China*
[5]*Department of Mechanical Engineering, University of Rochester, Rochester, New York 14627, USA*
[6]*Department of Physics and Astronomy, University of Rochester, Rochester, New York 14627, USA*

(Received 13 November 2022; accepted 14 April 2023; published 5 May 2023)

We propose an efficient way of axial magnetic fields generation in a nonrelativistic laser intensity regime by using a twisted light carrying orbital angular momentum (OAM) to stimulate two-plasmon decay (TPD) in a plasma. The growth of TPD driven by an OAM light in a Laguerre-Gauss (LG) mode is investigated through three-dimensional fluid simulations and theory. A theory based on the assumption that the electron plasma waves (EPWs) are locally driven by a number of local plane-wave lasers predicts the maximum growth rate proportional to the peak amplitude of the pump laser field and is verified by the simulations. The OAM conservation during its transportation from the laser to the TPD daughter EPWs is shown by both the theory and the simulations. The theory predicts generation of ≈40 T axial magnetic fields through the OAM absorption via TPD, which has perspective applications in the field of high energy density physics.

DOI: 10.1103/PhysRevResearch.5.L022025

Absorption of angular momentum from an intense twisted laser that carries orbital angular momentum (OAM) [1] can lead to the generation of strong axial magnetic fields in a plasma. This so-called inverse Faraday effect for OAM lasers [2] has recently attracted intensive research interest in relativistic-intensity ($I \gtrsim 10^{18}$ W/cm^2) laser plasma interactions [3–5]. At relatively lower intensities ($I \approx 10^{14}$–10^{16} W/cm^2) relevant to the leading facilities for inertial confinement fusion (ICF), an OAM laser is capable of passing its OAM selectively to electrons or ions in a plasma, in this regime via the laser plasma instability (LPI) processes [6–10], while little work has been reported on the axial magnetic field generation. When getting absorbed and decaying into a pair of daughter waves, an OAM laser is expected to transport OAM to its daughter waves via three-wave coupling due to angular-momentum conservation. Although both an electron plasma wave (EPW) [11–14] and an ion-acoustic wave (IAW) [15] can appear as a Laguerre-Gauss (LG) mode that carries OAM in a plasma, the OAM absorption from a laser into such a wave through LPI is not that efficient. The OAM transportation in paraxial LPI scenarios for stimulated Raman scattering or stimulated Brillouin scattering (SRS or SBS), whose two daughter waves include a scattered light wave and an EPW or IAW has been analytically modeled and numerically simulated [5–7,10]. In these studies, to ensure angular momentum being passed from a LG pump laser to an EPW or IAW, the daughter light wave needs to be seeded in a LG mode that already carries OAM and is launched collimated with the axis of the pump laser. The other EPW or IAW daughter wave in a paraxial LG form is then beaten by the collimated pump and scattered light satisfying the matching conditions on frequencies, wave vectors, and the azimuthal indices representing OAM [5–7,10]. However, SRS driven from thermal noise without such a LG-form seed demonstrates that virtually no angular momentum is transported to the daughter EPW while only the scattered light wave carries OAM [8].

These pioneering studies prompt two-plasmon decay (TPD) as an efficient candidate favoring the OAM absorption into the electrons of a plasma. TPD is a fundamental LPI process occurring when an electromagnetic wave decaying into a pair of EPWs [16,17] in the region where the electron number density is below 1/4 of the critical density (n_{cr}), above which a laser beam is not able to propagate. TPD is identified as a critical concern in ICF for its low threshold [16,18,19] and fuel-preheating risk caused by the energetic electrons it generates. Since both daughter waves of TPD are EPWs, the OAM carried by the pump laser is able to go nowhere else but into the daughter EPWs due to the angular-momentum conservation. TPD is intrinsically excited in a noncollimated way as the most unstable modes involve pairs of EPWs that propagate at fairly large angles with respect to the propagation direction of the pump laser [17]. This noncollimated geometry of the dominant modes is another key feature that would make TPD grow in a very distinguished way from the collimated forward or backward SRS or SBS in the previous OAM-SRS or OAM-SRS studies [6–8,10].

*ruiyan@ustc.edu.cn

In this Letter, we present the fluid simulations and theory on TPD growth driven by an OAM laser with moderate azimuthal indices in a homogeneous plasma, and propose a method to generate axial magnetic fields through TPD. We focus on the most common scenario where a LG pump laser shines in a plasma and stimulates TPD naturally from random noise. The laser intensities ($I \approx 10^{15}$ W/cm^2) are relevant to ICF experimental conditions. The EPWs are found to propagate at large angles with the axle of the incident laser and can be recognized approximately as a collection of enormous local planar plasma waves. A theory is then developed by decomposing the LG laser into local tilted plane waves which locally drive TPD EPWs via three-wave coupling. The TPD growth rate predicted by the theory well matches our simulation results for different azimuthal indices of the incident laser. This theory also predicts the angular momentum collectively carried by the EPWs, which excellently agrees with the simulation results and verifies the angular-momentum conservation in such a noncollimated LPI system. The EPWs collectively form a spiral current tube that generates axial magnetic fields whose magnitude is theoretically estimated. Intense axial static magnetic fields are beneficial to applications such as charged beam collimation [20], microscale pinch [21], and magnetized ICF [22]. Thanks to the encouraging progresses of the laser technology [9,23], OAM lasers at relevant intensities and an experimental validation could be expected in the near future.

We have performed a series of three-dimensional (3D) fluid simulations using our newly developed code FLAME-MD [24]. FLAME-MD solves the set of fluid-like equations presented in Ref. [25] in 3D space without taking envelopes in either space or time. The pump LG laser propagating along the z direction is prescribed in the vector potential in a standard form [1], which near the focus is approximated as

$$\mathbf{A}(x,y,z,t) = \frac{1}{2}\mathbf{A}_0\left[\frac{r\sqrt{2}}{w_{b0}}\right]^{|l|}\exp\left[-\frac{r^2}{w_{b0}^2}\right] \times \exp\left[i\omega_0 t - ik_0(z-z_0) + il\phi\right] + \text{c.c.}, \quad (1)$$

where $\mathbf{A}_0$ is the vector potential at the focus (x_0, y_0, z_0), $r \equiv [(x-x_0)^2 + (y-y_0)^2]^{1/2}$ is the radial distance to the laser axle, and w_{b0} is the waist on the focal plane. In addition, ω_0 and k_0 are its central frequency and wave number in plasma, ϕ and l are the azimuthal angle and the azimuthal index. The complex conjugate (c.c.) is added to make $\mathbf{A}$ real.

A typical simulation box is 22 μm (x)×22 μm (y)× 4.5 μm (z) with the grid of 2000×2000×400. The LG laser is focused at the center of box with $w_{b0} = 2.8$ μm. The LG laser whose central wavelength in vacuum is $\lambda = 0.351$ μm is linearly polarized along the y direction. A longer Rayleigh length ($z_R = 245$ μm) than physical for this spot size is set to mitigate the laser focusing effects near its waist while accommodating the computational costs. The module in FLAME-MD solving for the scattered lights is intentionally turned off to ensure that TPD is the only possible LPI in this scenario. A uniform electron density $n_0 = 0.23 n_{cr}$ is set with the electron temperature $T_e = 1.5$ keV. The ions are fixed and Landau damping is turned off, to make sure that TPD is growing

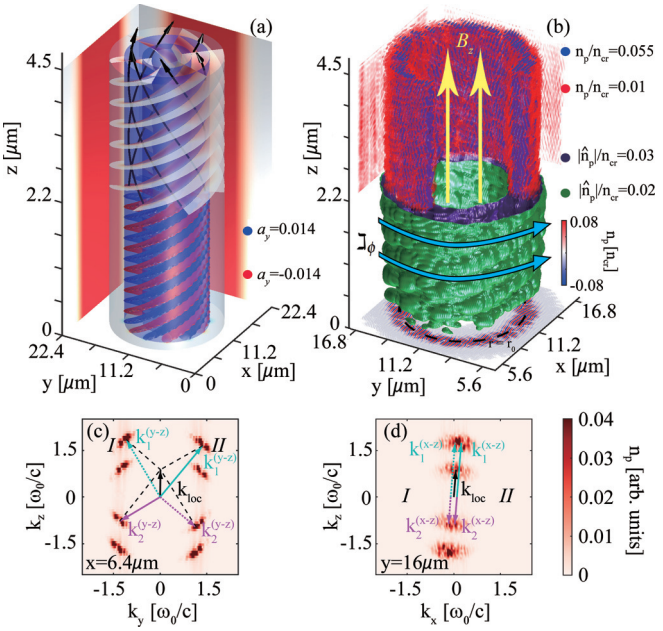

FIG. 1. LG laser profile with (a) $l = 6$ and (b)–(d) the electron density modulations (n_p) at $t = 0.75$ ps. (a) (upper half) Phase isosurfaces (white helical fronts) and the directions of the local Poynting vectors (black arrows). (lower half) Isosurfaces (red and blue) of the normalized vector potential ($a_y = eA_y/m_e c^2$). The white and light blue transparent cylinders show two intensity iso-surfaces. (b) (upper half) n_p isosurfaces with a quarter segment cut away. (lower half) Isosurfaces of enveloped n_p ($\hat{n}_p$). The bottom projection shows n_p on the focal plane, overlaid by the dashed circle $r = r_0$ where $a_{\max}$ is reached. The collective azimuthal current and the axial magnetic fields induced are marked by the blue and yellow arrows, respectively. Spectra of n_p on (c) a y-z slice passing Point A and on a (d) x-z slice passing Point C of Fig. 2(a). The arrows illustrate the TPD wave vector matching geometry projected on the slices for two pairs of dominant EPWs [I(dotted) and II(solid)].

in its linear (exponentially growing) phase without nonlinear saturation mechanisms involved.

A series of simulations with moderate l ranging from zero to six are performed. The case with $l = 0$ retreats to a regular Gaussian laser carrying no OAM. For a fair comparison on TPD growth that was found sensitive to the local maximum laser electric field [19], the maximum vector potential's magnitude ($A_{\max}$) normalized as $a_{\max} = eA_{\max}/(m_e c^2) = 0.024$ is set identical for different l cases. Here e is the electron charge, m_e the electron mass, and c the light speed in vacuum. The maximum laser intensity associated with $a_{\max} = 0.024$ is $I_{\max} = 6.5\times10^{15}$ W/cm^2 via $a_{\max} = 0.0085(I_{14}^{\max}\lambda_{\mu m}^2)^{1/2}$, where $I_{14}^{\max}$ is $I_{\max}$ in 10^{14} W/cm^2, and $\lambda_{\mu m}$ is λ in μm, respectively.

The contour of a of the pump laser in the $l = 6$ case is illustrated in the lower half of Fig. 1(a) while the vortex property of the local Poynting vectors perpendicular to the helical wavefronts are marked as arrows in the upper half of Fig. 1(a). A global scope of the EPWs stimulated in the same case is illustrated in Fig. 1(b). The upper half shows the electron-density modulations due to EPWs (n_p) and the lower half shows an envelope of n_p. It is shown that the EPWs are

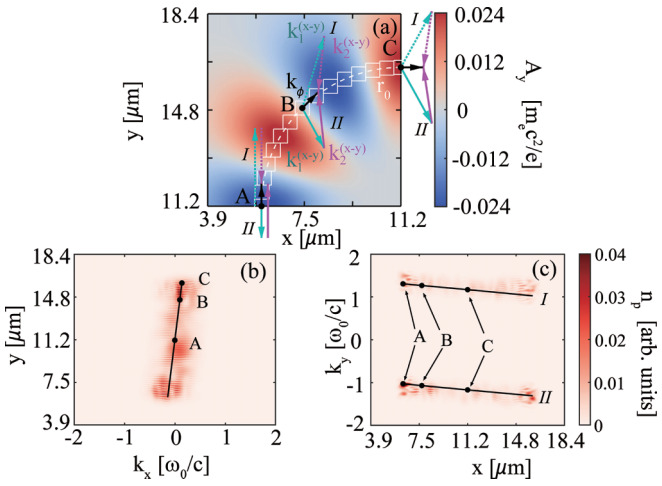

FIG. 2. (a) A_y on its focal plane in the simulation with $l = 6$ at $t = 0.75$ ps. The white squares are the schematic of the zones S_n on the cylinder $r_n = r_0$ (dashed). The arrows are the x-y projections of $\mathbf{k}_{\rm loc}$ (black), $\mathbf{k}_1$ (purple), and $\mathbf{k}_2$ (cyan) at three locations (A, B, and C), respectively. The dotted and solid arrows at A, B, and C show the wave vector matching geometry of the two pairs of dominant EPWs (I, II), respectively. n_p spectra in (b) k_x-y and (c) k_y-x spaces overlaid by the theoretical prediction of the dominant $\mathbf{k}_1$ using Eq. (7) (solid line) with the values at A, B, and C marked in black dots. Only the EPWs with $\mathbf{k}_1$ are shown in the spectra.

concentrated on a hollow cylinder near $r = r_0 \equiv w_{b0}\sqrt{|l|/2}$ where the pump laser reaches its radial peak intensity ($r_0 =$ 4.8 μm for $l = 6$). The spectra of n_p on two slices tangent to the cylinder of $r = r_0$ are shown in Figs. 1(c) and 1(d). Two pairs of dominant EPWs (I, II) are found to propagate at large angles with respect to the laser propagation direction on the y-z slice where the laser is polarized [see Fig. 1(c)] within this plane, while these dominant EPWs are concentrated at small k_x on the x-z slice [see Fig. 1(d)]. These EPWs' structure largely at odds with a paraxial LG mode are similar to these in the simulations of plane-wave-laser-driven TPD [26,27].

To model the growth of TPD driven by a LG laser with arbitrary OAM states, we have developed a theory based on the EPWs' features in the simulations. The EPWs originated from thermal noise can be approximately recognized as a number of local planar waves stimulated by local plane-wave pumps via TPD. Correspondingly, we can divide the space into numerous small zones (S_n, $n = 1, 2, \ldots$) in each of which the piece of the LG laser is approximated by a plane wave. S_n looks like a fine rod parallel to the z axis and has a small cross section centered at (x_n, y_n) on the x-y plane. The zones on $r = r_0$ are illustrated by the squares in Fig. 2(a). The laser field on the large Rayleigh-length limit ($z \ll z_R$) can be described piecewise by Taylor expanding Eq. (1) on (x_n, y_n) in each individual zone, i.e.,

$$\mathbf{A}(x, y, z, t) = \sum^{n} \frac{1}{2}\mathbf{A}_n T_n(x', y')(1 + P_{xn}x' + P_{yn}y') \times \exp[ik_{yn}y' + ik_{xn}x' - ik_0(z - z_0)] + O(x'^2, y'^2) + \text{c.c.}, \quad (2)$$

where $\mathbf{A}_n \equiv \mathbf{A}(x_n, y_n, z_0, t)$, $x' \equiv x - x_n$, $y' \equiv y - y_n$, T_n is a flat-top window function such that $T_n(x', y') = 1$ when $(x, y, z) \in S_n$ and zero otherwise, $P_x = x_n(l w_{b0}^2 - 2r_n^2)/(w_{b0}^2 r_n^2)$, $P_y = y_n(l w_{b0}^2 - 2r_n^2)/(w_{b0}^2 r_n^2)$, $r_n = [(x_n - x_0)^2 + (y_n - y_0)^2]^{1/2}$ is the radius of each zone's center to the laser axle, $k_{xn} = \sin\phi_n l/r_n$, $k_{yn} = -\cos\phi_n l/r_n$, $\phi_n = \arctan[(y_n - y_0)/(x_n - x_0)]$ is ϕ in Eq. (1) evaluated at (x_n, y_n). The leading terms of Eq. (2) sketch inside each zone a local plane wave propagating at $\mathbf{k}_{\rm loc} = (k_{xn}, k_{yn}, k_0)^T \equiv \mathbf{k}_\phi + \mathbf{k}_0$, which is illustrated by the wave vector-matching-condition triangles in Figs. 1(c) and 1(d).

As EPWs are assumed locally driven via TPD in each zone in this model, the fastest growing modes are determined by the zones [see Fig. 2(a)] illuminated at the highest laser intensity, i.e., $r_n = r_0$ where $\mathbf{A}_n = \mathbf{A}_{\max} = \mathbf{A}_0 \exp[-|l|/2]|l|^{(|l|/2)}$. Besides, $r_n = r_0$ leads to $P_{xn} = P_{yn} = 0$, indicating a uniform laser intensity in the zone to first-order accuracy. Inside such a zone, the differential equations governing TPD growth can be written as [16,28]

$$\frac{\partial\psi}{\partial t} = \frac{e}{m_e}\phi - 3v_e^2\frac{n_p}{n_0} - \mathbf{v}_0 \cdot \nabla\psi, \quad (3)$$

$$\frac{\partial n_p}{\partial t} = -n_0\nabla^2\psi - \mathbf{v}_0 \cdot \nabla n_p, \quad (4)$$

$$\nabla^2\phi = -4\pi e n_p, \quad (5)$$

where ψ is the velocity potential, ϕ the electrostatic potential, v_e the electron thermal velocity, $\mathbf{v}_0 = e\mathbf{A}_{\max}/m_e c$ the electron oscillation velocity. The variables (i.e., ψ, n_p, or ϕ) can be written as combinations of two well-defined daughter waves, $\{\psi, n_p, \phi\} \equiv (1/2)\{\Psi_1, N_{p1}, \Phi_1\}\exp[i(\mathbf{k}_1 \cdot \mathbf{r} - \omega_1 t)] + (1/2)\{\Psi_2, N_{p2}, \Phi_2\}\exp[i(\mathbf{k}_2 \cdot \mathbf{r} - \omega_2 t)] + \text{c.c.}$, where ω_1, ω_2, $\mathbf{k}_1$, $\mathbf{k}_2$ are the EPWs' frequencies and wave vectors satisfying the matching conditions $\mathbf{k}_{\rm loc} = \mathbf{k}_1 + \mathbf{k}_2$ and $\omega_0 = \omega_1 + \omega_2$. Equations (3)–(5) can be cast into a standard form of the three-wave coupling model [28] as $[\partial_t + v_{z1,z2}\partial_z]a_{1,2} = \gamma_0 a_{2,1}^*$, where $a_{1,2} \equiv (|k_{y1,y2}v_0||\omega_{1,2}/\omega_{2,1} - k_{1,2}^2/k_{2,1}^2|/4)^{1/2}\Phi_{1,2}$, v_{z1} and v_{z2} are the z components of the EPWs' group velocities, and k_{y1} and k_{y2} are the y components of $\mathbf{k}_1$ and $\mathbf{k}_2$. Without losing generality, the higher-frequency wave in the paired daughter EPWs are denoted by subscript 1. The TPD growth rate is given by the coupling coefficient γ_0:

$$\gamma_0 = \sqrt{\frac{1}{16}k_\perp^2 v_0^2\left(\frac{\omega_2}{\omega_1} - \frac{k_2^2}{k_1^2}\right)\left(\frac{\omega_1}{\omega_2} - \frac{k_1^2}{k_2^2}\right)}, \quad (6)$$

where $k_\perp \equiv |k_{y1} - k_{y2}|/2$. The factor $k_\perp^2$ in Eq. (6) has been approximated from $|k_{y1}k_{y2}|$ by neglecting the second-order term of k_{yn} as $|k_{y1}k_{y2}| = k_\perp^2 - k_{yn}^2/4$ and $|k_{yn}| \ll k_0$. The dominant EPW pairs which maximize γ_0 can be found in each zone using Eq. (6) and the matching conditions. The same maxima of γ_0 in all zones on $r = r_0$ are expected to be reached at the same values of k_1, k_2, and $k_\perp^2$, while different $\mathbf{k}_\phi$ [see Points A–C in Fig. 2(a)] causes different directions of $\mathbf{k}_1$ in each zone. The dominant $\mathbf{k}_1$ is located within the plane determined by $\mathbf{k}_{\rm loc}$ and the polarization (y) direction.

The dominant EPW's $\mathbf{k}_1$ in each zone can be calculated as a rotation of $\mathbf{k}_{\rm norm}$, which is the dominant $\mathbf{k}_1$ driven by a plane-wave laser polarized along y and propagating along z with the wave vector $(k_0^2 + k_\phi^2)^{1/2}$. It is numerically found

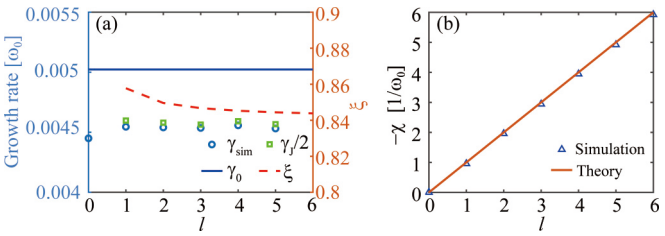

FIG. 3. (a) Comparison of growth rates under the same A_{max}. γ_0 is theoretically predicted by Eq. (6). γ_{sim} and γ_J are the growth rates of the EPWs' amplitude and angular momentum fitted with the simulation data, respectively. (b) Comparison of $-X$ of the TPD EPWs in the theory and the simulations.

that $k_{norm} = (0, \pm 1.23, 1.75)^T \omega_0/c$ for the particular n_e and T_e in our cases. Since a plane-wave laser drives two pairs of EPWs symmetrically on both sides, $\mathbf{k}_{norm}$ has two values. The rotation can be described as $\mathbf{k}_1 = \mathbf{M}_{xy} \cdot \mathbf{k}_{norm}$, where $\mathbf{M}_{xy}$ is the rotation tensor written as a product of two matrices,

$$\mathbf{M}_{xy} = \begin{bmatrix} \cos\varphi_1 & 0 & \sin\varphi_1 \\ 0 & 1 & 0 \\ -\sin\varphi_1 & 0 & \cos\varphi_1 \end{bmatrix} \begin{bmatrix} 1 & 0 & 0 \\ 0 & \cos\varphi_2 & \sin\varphi_2 \\ 0 & -\sin\varphi_2 & \cos\varphi_2 \end{bmatrix}. \tag{7}$$

$\varphi_1 = \arctan(k_{xn}/k_0)$ is the angle between $\mathbf{k}_{loc}$ and the x axis, and $\varphi_2 = \arcsin[k_{yn}/(k_{xn}^2 + k_0^2)^{1/2}]$ is the angle between $\mathbf{k}_{loc}$ and its projection on the x-z plane. A very good agreement between the theory and the simulation on the dominant EPW's $\mathbf{k}_1$ is shown in Figs. 2(b) and 2(c).

Substituting the dominant EPWs' information into Eq. (6) yields the maximum of $\gamma_0 = 0.005\omega_0$ which does not depend on l but only on A_{max}. In Fig. 3(a) γ_0 is compared with γ_{sim} that is measured as half of the growth rate of the volume integral of n_p^2 over the entire simulation domain for different l. Although γ_{sim} is contributed by all TPD modes with different growth rates, it is determined by the dominant modes with the fastest growth after adequately long time in this linearly growing system. Good agreement of γ_0 and γ_{sim} is shown in Fig. 3(a) as the relative errors are within 10%. The weak dependence of γ_{sim} on l also confirms that A_{max} is the key factor determining TPD growths. $\xi(l) \equiv A_{max}^{LG}/A_{max}^{Gauss}$ as the ratio of A_{max} between a LG laser and a Gaussian laser with an identical energy flux and under the same plasma conditions can be used to evaluate the TPD mitigation efficacy for different l. By using Eq. (1), ξ can be readily found as

$$\xi(l) = \sqrt{\frac{\sqrt{\pi}|l|^{|l|}}{\Gamma\left(|l| + \frac{1}{2}\right)}} \exp\left(-\frac{|l|}{2}\right), \tag{8}$$

The values of ξ at $l = 1, 2, \ldots, 6$ are plotted in Fig. 3(a). It is shown that γ_0 is reduced by roughly 15% if the pump is switched from a Gaussian beam [$\xi(0) = 1$] to a LG beam within this range of l (1–6) while maintaining the same laser power, which suggests LG lasers as a pump candidate in direct-drive ICF for TPD mitigation.

The TPD EPWs collectively carry an angular momentum along z. Again consider the fastest growing modes located in the zones near $r = r_0$ which will dominate the angular momentum. The angular-momentum density ($\mathbf{j}_n$) of the EPWs in the nth zone can be expressed as $\mathbf{j}_n = \mathbf{r}_n \times \mathbf{p}_n$, where $\mathbf{p}_n = m_e(\hat{n}_{p1}^{*I}\hat{\mathbf{v}}_{e1}^{I} + \hat{n}_{p2}^{*I}\hat{\mathbf{v}}_{e2}^{I} + \hat{n}_{p1}^{*II}\hat{\mathbf{v}}_{e1}^{II} + \hat{n}_{p2}^{*II}\hat{\mathbf{v}}_{e2}^{II})/4 + \text{c.c.}$ is the time-averaged electron momentum density. $\hat{\mathbf{v}}_{e1,2} = \omega_{1,2}\mathbf{k}_{1,2}a_{1,2}/(4\pi e n_0 \alpha_{1,2})$ and $\hat{n}_{p1,2} = -k_{1,2}^2 a_{1,2}/(4\pi e \alpha_{1,2})$ are the enveloped values of the microscopic velocity $\mathbf{v}_e$ and n_p associated with each EPW, respectively. In each zone two dominant pairs of TPD daughter waves which have the same growth rate γ_0 are allowed to grow from independent initial conditions. The solution of the three-wave model describing an absolute growth of the two pairs of daughter waves in the nth zone is $a_1^{I,II} = \tilde{a}_n^{I,II}\exp(\gamma_0 t)$ and $a_2^{I,II} = \tilde{a}_n^{*I,II}\exp(\gamma_0 t)$, where $\tilde{a}_n$ are determined by the initial conditions, i.e., the local thermal noise. As the dominant EPWs at zones on $r = r_0$ have the same values of γ_0, ω_1, ω_2 and k_1, k_2 the leading term of the angular momentum per unit length in z can be readily obtained by summing up all the zones as

$$J_z = -\frac{l\omega_1\omega_2}{2\pi\omega_{pe}^2}\frac{\exp(2\gamma_0 t)}{k_\perp v_0\left|\frac{\omega_2}{k_2^2} - \frac{\omega_1}{k_1^2}\right|}\sum_{n,r=r_0}\left[\tilde{a}_n^I\tilde{a}_n^{*I} + \tilde{a}_n^{II}\tilde{a}_n^{*II}\right]\Delta\sigma_n, \tag{9}$$

where $\omega_{pe} = (4\pi n_0 e^2/m_e)^{1/2}$ is the electron plasma frequency and $\Delta\sigma_n$ is the cross-sectional area on the x-y plane of S_n. Equation (9) predicts an exponential growth of J_z with a growth rate $2\gamma_0$, which has been verified by our simulations and plotted in Fig. 3(a). J_z of EPWs in the simulations is calculated by integrating $\mathbf{r}\times m_e n_p \mathbf{v}_e$ over the x-y plane and then averaging it over z.

To bridge the angular momentum carried by the TPD EPWs and by the pump laser, a quantity X describing angular momentum over energy is introduced as $X \equiv J_z/W$, where W is the waves' energy per unit length in z. It was found that $X_{pump} = -l/\omega_0$ for a linearly polarized LG laser [1], consistent with the fact that this LG light has an OAM of $-l\hbar$ per photon. In our theory the leading term of the EPWs' total energy can be expressed as a sum of the dominant EPWs' energies in all of the zones on $r = r_0$, ie., $W_{EPW} = \sum_n (w_{n1}^I + w_{n2}^I + w_{n1}^{II} + w_{n2}^{II})\Delta\sigma_n$, where $w_{n1,2}^{I,II} = \omega_{1,2}^2 k_{1,2}^2 a_{1,2}^{I,II} a_{1,2}^{*I,II}/(8\pi\omega_{pe}^2\alpha_{1,2}^2)$ (reformed Eq. 10 of Ref. [29]) is the energy density of the two pairs of dominant EPWs respectively in the nth zone. Using Eq. (9) one can readily obtain $X_{EPW} = -l/\omega_0 = X_{pump}$. In our simulations, X_{EPW} averaged over the simulation box are plotted in Fig. 3(b) and they precisely match the theory. Identical X values for the pump laser and the TPD EPWs guarantee the angular momentum conservation during the TPD process since the energy is known to be conserved.

The TPD EPWs collectively form a spiral current tube [see Fig. 1(a)] that generates collimated axial magnetic fields (B_z) inside the tube. Precise modeling on the evolution of B_z requires kinetic simulations. Here we give an estimate on the quasistatic B_z based on the assumption that TPD is saturated such that the time-averaged azimuthal current density $\mathfrak{J}_\phi$ reaches a quasistatic value. Then B_z can be calculated as $B_z(r) = (4\pi/c)\int_r^\infty \mathfrak{J}_\phi dr'$ [5], where $\mathfrak{J}_\phi$ is correlated with J_z as $J_z = (-m_e/e)\int_0^{2\pi} d\phi \int_0^\infty r^2 \mathfrak{J}_\phi dr$. Under the approximation that $\mathfrak{J}_\phi$ is uniformly distributed on a thin tube around $r = r_0$, the maximum (B_{max}) of B_z reached inside the tube can be expressed as $B_{max} = -2eJ_z/(m_e c r_0^2) \approx$

$elD_{\rm tube}\bar{E}^2_{\rm EPW}/(4m_e c\omega_p r_0)$, where $D_{\rm tube}$ is the thickness of the current tube and $\bar{E}_{\rm EPW}$ is the averaged electric field amplitude due to EPWs. $D_{\rm tube}$ can be approximated by the full-width-half-maximum of the laser amplitude peak at $r = r_0$, ie., $D_{\rm tube} \approx 1.2w_{b0}$. The saturated level of $\bar{E}_{\rm EPW}$ is determined by complicated nonlinear effects absent in our fluid simulations and is still an open question. However, based on our kinetic simulations on plane-wave-laser-driven TPD [26,30,31], the saturated $\bar{E}_{\rm EPW}$ were found larger than the laser electric fields in most cases. A lower limit of $\bar{E}_{\rm EPW}$ is arguably estimated as $\omega_0 A_{\rm max}/c$, which yields an estimation on $B_{\rm max}$ formulated in practical units.

$$B_{\rm max} \gtrsim 0.7 I_{14}^{\rm max} \lambda_{\mu m} \sqrt{l}\,[\rm T]. \tag{10}$$

In the case of $l = 6$, Eq. (10) predicts generation of about 40 T quasistatic axial magnetic field via this LG-laser-driven TPD process, same order of magnitude as predicted by the theories in Refs. [4,5] in the relativistic-laser-intensity regime. Our mechanism also demonstrates pure laser-driven generation of axial magnetic fields with amplitudes that are similar to the method using a pulsed-power-driven coil [22]. Important topics such as nonlinear TPD saturation and multi LPI modes competition are beyond the scope of this Letter and should be studied with kinetic simulations in future works.

This research was supported by the Strategic Priority Research Program of Chinese Academy of Sciences, Grants No. XDA25050400 and No. XDA25010200, by the National Natural Science Foundation of China (NSFC) under Grants No. 12175229 and No. 11621202, and by the Fundamental Research Funds for the Central Universities. The numerical calculations in this paper have been done on the supercomputing system in the Supercomputing Center of University of Science and Technology of China.

[1] L. Allen and M. J. Padgett, The Poynting vector in Laguerre-Gaussian beams and the interpretation of their angular momentum density, Opt. Commun. **184**, 67 (2000).

[2] S. Ali, J. R. Davies, and J. T. Mendonca, Inverse Faraday Effect with Linearly Polarized Laser Pulses, Phys. Rev. Lett. **105**, 035001 (2010).

[3] A. Longman and R. Fedosejevs, Kilo-tesla axial magnetic field generation with high intensity spin and orbital angular momentum beams, Phys. Rev. Res. **3**, 043180 (2021).

[4] R. Nuter, P. Korneev, E. Dmitriev, I. Thiele, and V. T. Tikhonchuk, Gain of electron orbital angular momentum in a direct laser acceleration process, Phys. Rev. E **101**, 053202 (2020).

[5] Y. Shi, J. Vieira, R. M. G. M. Trines, R. Bingham, B. F. Shen, R. J. Kingham *et al.*, Magnetic Field Generation in Plasma Waves Driven by Copropagating Intense Twisted Lasers, Phys. Rev. Lett. **121**, 145002 (2018).

[6] J. T. Mendonça, B. Thidé, and H. Then, Stimulated Raman and Brillouin Backscattering of Collimated Beams Carrying Orbital Angular Momentum, Phys. Rev. Lett. **102**, 185005 (2009).

[7] J. Vieira, R. M. Trines, E. P. Alves, R. Fonseca, J. Mendonça, R. Bingham, P. Norreys, and L. Silva, Amplification and generation of ultra-intense twisted laser pulses via stimulated Raman scattering, Nat. Commun. **7**, 10371 (2016).

[8] R. Nuter, P. Korneev, and V. Tikhonchuk, Raman scattering of a laser beam carrying an orbital angular momentum, Phys. Plasmas **29**, 062101 (2022).

[9] W. Gao, C. Mu, H. Li, Y. Yang, and Z. Zhu, Parametric amplification of orbital angular momentum beams based on light-acoustic interaction, Appl. Phys. Lett. **107**, 041119 (2015).

[10] Q. Feng, R. Aboushelbaya, M. Mayr, W. Wang, R. Trines, B. Spiers, R. Paddock, I. Ouatu, R. Timmis, R. Wang *et al.*, Efficient generation of new orbital angular momentum beams by backward and forward stimulated Raman scattering, arXiv:2202.00105.

[11] J. T. Mendonca, S. Ali, and B. Thidé, Plasmons with orbital angular momentum, Phys. Plasmas **16**, 112103 (2009).

[12] D. R. Blackman, R. Nuter, P. Korneev, and V. T. Tikhonchuk, Twisted kinetic plasma waves, J. Russ. Laser Res. **40**, 419 (2019).

[13] D. R. Blackman, R. Nuter, P. Korneev, and V. T. Tikhonchuk, Kinetic plasma waves carrying orbital angular momentum, Phys. Rev. E **100**, 013204 (2019).

[14] D. R. Blackman, R. Nuter, P. Korneev, A. Arefiev, and V. Tikhonchuk, Kinetic phenomena of helical plasma waves with orbital angular momentum, Phys. Plasmas **29**, 072105 (2022).

[15] M. Ayub, S. Ali, and J. Mendonca, Phonons with orbital angular momentum, Phys. Plasmas **18**, 102117 (2011).

[16] C. S. Liu and M. N. Rosenbluth, Parametric decay of electromagnetic waves into two plasmons and its consequences, Phys. Fluids **19**, 967 (1976).

[17] W. Kruer, *The Physics of Laser Plasma Interactions* (Westview Press, Boulder, 2003).

[18] A. Simon, R. W. Short, E. A. Williams, and T. Dewandre, On the inhomogeneous two-plasmon instability, Phys. Fluids **26**, 3107 (1983).

[19] C. Lian, Y. Ji, R. Yan, S. Cao, C. Ren, Z. Wan, D. Yang, Y. Ding, and J. Zheng, Two plasmon decay instability stimulated by large-incidence-angle laser in inertial confinement fusion, Plasma Phys. Control. Fusion **64**, 085009 (2022).

[20] Z. Sheng, J. Meyer-ter Vehn, and A. Pukhov, Analytic and numerical study of magnetic fields in the plasma wake of an intense laser pulse, Phys. Plasmas **5**, 3764 (1998).

[21] V. Kaymak, A. Pukhov, V. N. Shlyaptsev, and J. J. Rocca, Nanoscale Ultradense *Z*-Pinch Formation from Laser-Irradiated Nanowire Arrays, Phys. Rev. Lett. **117**, 035004 (2016).

[22] J. D. Moody, B. B. Pollock, H. Sio, D. J. Strozzi, D. D.-M. Ho, C. A. Walsh, G. E. Kemp, B. Lahmann, S. O. Kucheyev, B. Kozioziemski, E. G. Carroll, J. Kroll, D. K. Yanagisawa, J. Angus, B. Bachmann, S. D. Bhandarkar, J. D. Bude, L.

Divol, B. Ferguson, J. Fry *et al.*, Increased Ion Temperature and Neutron Yield Observed in Magnetized Indirectly Driven D_2-Filled Capsule Implosions on the National Ignition Facility, Phys. Rev. Lett. **129**, 195002 (2022).

[23] W. P. Wang, C. Jiang, H. Dong, X. M. Lu, J. F. Li, R. J. Xu, Y. J. Sun, L. H. Yu, Z. Guo, X. Y. Liang *et al.*, Hollow Plasma Acceleration Driven by a Relativistic Reflected Hollow Laser, Phys. Rev. Lett. **125**, 034801 (2020).

[24] F. Zhou, S. Cao, C. Lian, Y. Ji, R. Yan, J. Li, D. Yang, L. Hao, C. Ren, and J. Zheng, Large-incidence-angle multiple-beam two-plasmon decay instability in inertial confinement fusion (unpublished).

[25] L. Hao, R. Yan, J. Li, W. Liu, and C. Ren, Nonlinear fluid simulation study of stimulated Raman and Brillouin scatterings in shock ignition, Phys. Plasmas **24**, 062709 (2017).

[26] R. Yan, Two-plasmon-decay instability and energetic electron generation in direct-drive inertial confinement fusion, Ph.D. thesis, University of Rochester, 2012.

[27] H. Wen, A. Maximov, R. Short, J. Myatt, R. Yan, and C. Ren, Two-plasmon decay instability in inhomogeneous plasmas at oblique laser incidence, Phys. Plasmas **23**, 092713 (2016).

[28] R. Yan, A. Maximov, and C. Ren, The linear regime of the two-plasmon decay instability in inhomogeneous plasmas, Phys. Plasmas **17**, 052701 (2010).

[29] K. Y. Bliokh and Y. P. Bliokh, Momentum, angular momentum, and spin of waves in an isotropic collisionless plasma, Phys. Rev. E **105**, 065208 (2022).

[30] R. Yan, A. V. Maximov, C. Ren, and F. S. Tsung, Growth and Saturation of Convective Modes of the Two-Plasmon Decay Instability in Inertial Confinement Fusion, Phys. Rev. Lett. **103**, 175002 (2009).

[31] R. Yan, C. Ren, J. Li, A. V. Maximov, W. B. Mori, Z. M. Sheng, and F. S. Tsung, Generating Energetic Electrons Through Staged Acceleration in the Two-Plasmon-Decay Instability in Inertial Confinement Fusion, Phys. Rev. Lett. **108**, 175002 (2012).